Experimental Verification With Loads of Line-Start Type Self-Excited Wound-Field Motor With Three-Phase Concentrated Winding Stators

Masahiro Aoyama, *Member, IEEE*, Mitsuru Saito, Takahiro Mizuta, Yoshihiro Miyama, *Member, IEEE*, and Kazumasa Ito

***Abstract*—This article describes a novel line-start type self-excited wound-field synchronous motor with three-phase concentrated winding stator. The unique feature of this proposed motor is that it accelerates by obtaining the starting torque from the slip frequency at the time of starting, and at the time of synchronous pull-in, it is driven synchronously with utilizing the second order space harmonic as the field magnetization power. This driving principle was verified by performing a load test using the prototype with two types of load, fan load and eddy current brake load. Consequently, the synchronization based on the proposed drive principle could be demonstrated on the actual machine, and the line-start characteristics of the proposed motor have been clarified.**

***Index Terms*—Brushless wound-field, concentrated winding stator, line-start, self-excitation, synchronization.**

I. Introduction

CONVENTIONALLY an induction motor (IM) capable of self-starting by directly connecting a commercial AC power supply has been widely used as a general-purpose industrial motor having a fan or a pump as a load due to a demand for cost reduction of its system. Induction machines are low in cost because of drive systems that do not require inverters or sensors, but on the other hand, they require an excitation current to obtain field magnetic flux, making it more difficult to achieve higher efficiency. Efficiency can be improved by using a permanent magnet synchronous motor (PMSM) that does not require an excitation current, but an inverter is indispensable because a PMSM cannot in principle start by itself. Therefore, it has not been widely used in industrial applications from the viewpoint of system cost. Therefore, research on a line-start type permanent magnet synchronous motor (LS-PMSM) having a self-starting function by embedding a secondary conductor on the outer periphery of the rotor has been advanced [1]–[8]. In recent years, an axial-gap structure or dual stator structure has been studied for the purpose of improving the torque density of the LS-PMSM [9]–[11]. This type of motor has high output and high efficiency at the time of synchronization. On the other hand, there are problems such as a brake torque caused by the permanent magnet flux while driving asynchronously. And immediately after starting, a large AC magnetic flux corresponding to the slip frequency is linked to the magnet, so there is a risk of demagnetization of the magnet [12], [13]. Further, there is a problem that it is difficult to reduce the armature copper loss due to the distributed winding stator structure. In order to prevent these problems, there are techniques such as adopting a high coercive force magnet with a large amount of rare earth such as Dy or Tb added, or a distributed winding stator structure using a preformed rectangular wire bar preformed to shorten the coil-end and reduce the resistance value. However, the cost increases [14]. Another study, although the design concept is different, as a first one, a brushless wound-field type three-phase synchronous motor that self-starts by using Gerges phenomenon at the time of starting is reported [15]. However, there are structural restrictions such as the need to incorporate a line-start winding in the stator and a switch for switching between the line-start winding and the armature winding. As a second study, a line-start type synchronous reluctance motor (LS-SynRM) in which a secondary conductor is embedded in a multilayer flux barrier has been reported [16]–[25]. Since torque can be generated by synchronous reluctance torque during synchronization, secondary copper loss can be reduced during synchronization. However, in addition to the need for an excitation current to obtain a field flux as in the case of the IM, it is difficult to reduce the armature copper loss due to the distributed winding stator structure.

In viewpoint of the above problems, the authors have developed a concentrated winding stator structure type LS-motor that can reduce the armature copper loss and the motor size. In addition, we are studying the possibility of a motor that can achieve higher performance than IM under the constraint that magnets are free, and no active elements are used. This paper

Manuscript received May 26, 2020; revised August 1, 2020; accepted September 8, 2020. Date of publication September 18, 2020; date of current version May 21, 2021. *(Corresponding author: Masahiro Aoyama.)*

Masahiro Aoyama is with the Shizuoka University, Hamamatsu, Shizuoka 432-8561, Japan (e-mail: aoyama.masahiro@shizuoka.ac.jp).

Mitsuru Saito is with the Shizuoka University, Hamamatsu, Shizuoka 432-8561, Japan. He is now with Nagoya Institute of Technology, Nagoya, Aichi 466-8555, Japan (e-mail: m.saito.173@stn.nitech.ac.jp).

Takahiro Mizuta and Kazumasa Ito are with the Advanced Technology R&D Center, Mitsubishi Electric Corporation, Amagasaki, Hyogo 661-8661, Japan (e-mail: mizuta. takahiro@dy.mitsubishielectric.co.jp; ito.kazumasa@cb.mitsubishielectric.co.jp).

Yoshihiro Miyama is with the Advanced Technology R&D Center, Mitsubishi Electric Corporation,. He is now with the Himeji Works, Mitsubishi Electric Corporation, Himeji, Hyogo 670-0993, Japan (e-mail: yoshihiro@bc.mitsubishielectric.co.jp).

Color versions of one or more of the figures in this article are available online at https://ieeexplore.ieee.org.

Digital Object Identifier 10.1109/TEC.2020.3025134

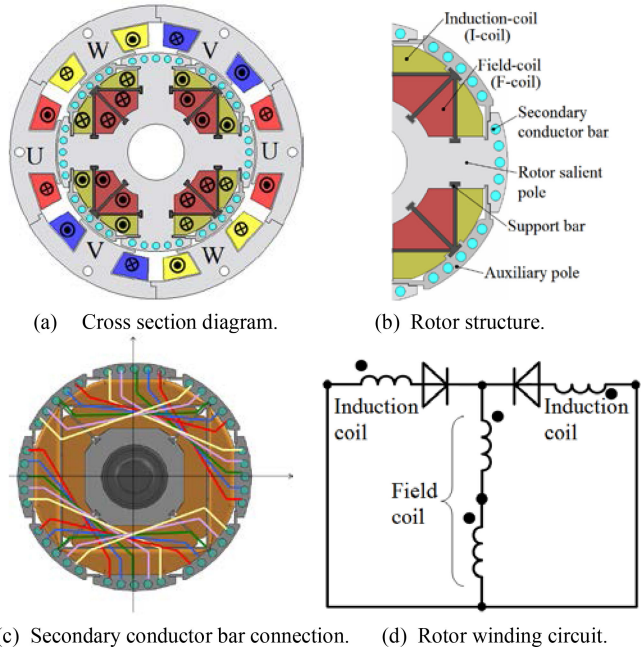

(a) Cross section diagram. (b) Rotor structure.

(c) Secondary conductor bar connection. (d) Rotor winding circuit.

Fig. 1. Proposed novel line-start machine.

presents a proposal of line-start type self-excited wound-field synchronous motor (LS-SEWFM) based on a new principle and the results of verifying the drive characteristics by performing a load test.

II. Novel Line-Start Machine Topology

A. Structure and Principle

Fig. 1(a) and (b) show radial cross sections of the proposed motor. It consists of a magnetic circuit in which two types of rotor windings are wound around the rotor having a forward salient pole structure and auxiliary poles are arranged between salient poles. The auxiliary pole is held structurally using a bar made with the Markforged CFRP 3-D printer. Forty secondary conductor bars are arranged on the rotor outer diameter side. The secondary conductor bars are short-circuited at the pitch of the number of poles as shown in Fig. 1(c), and the two short-circuited secondary conductor pairs are not connected to other pairs with electrically independent. In this research, because it is a 4-pole machine, the secondary conductor bars are short-circuited at a 4-pole pitch, so that the second order space harmonic shown in the next section are not magnetically coupled at the time of synchronization pull-in. The two types of rotor windings consist of an induction coil (I-coil) that obtains a magnetomotive force from the second order space harmonic that is unavoidable due to the concentrated winding stator structure, and a field coil (F-coil) that forms a field pole through a diode, and Fig. 1(d) shows the connection circuit. It is based on the self-excitation technique using the space harmonics of the Ref. [26], and the F-coil can be driven while forming an electromagnet utilizing space harmonic as a field energy source during synchronization. On the other hand, at the time of line-starting, it can be driven by the operation principle of IM by the secondary conductor bar. It means that immediately after line-start, this motor is accelerated by obtaining torque from the slip frequency, and at the time of synchronization, it is driven as a brushless wound-field type synchronous motor utilizing the second order space harmonic as a field energy source. The specifications are downsized from the required spec for the product in order to conduct experiments in the laboratory equipment in university. The main specifications are as shown in Table I.

TABLE I
Main Specifications of Prototype

Stator outer diameter (mm)	125
Stack length (mm)	80
Air gap length (mm)	0.65
Armature winding connection	2-parallel, Y-connection
Number of armature coil (turn/tooth)	100
Resistance of armature coil (Ω/tooth)	0.84
Number of induction coil (turn/pole)	41
Number of field coil (turn/pole)	104
Resistance of induction coil (Ω/pole)	0.33 (average)
Resistance of field coil (Ω/pole)	0.86 (average)
Resistance of secondary conductor bar (mΩ/bar)	0.61

B. Magnetic Circuit Design Concept

As mentioned in the previous chapter, this research aims to develop a motor that is magnet-free and can achieve higher performance than IM. The difference between IM, LS-SynRM and LS-PMSM is, as described above, whether or not it is necessary to intentionally supply the excitation current for obtaining the field magnetic flux from the armature side. As a case of research on a motor that self-starts other than IM, LS-SynRM, or LS-PMSM, there is a research report on a line-start type single-phase switched reluctance motor (LS-SRM) for the purpose of replacing single-phase IM in Ref. [27]. However, it is intended for small-output home electric appliances and is not suitable for industrial use because cost is more important than performance. Also, in the case of the SRM, similarly to the IM, it is necessary to supply the excitation current from the armature winding side, so that it is difficult to improve the efficiency.

As a technique that does not require intentionally supplying an excitation current from the armature side and realizes magnet-free, there is a self-excitation technique utilizing space harmonic described in the previous section. The self-excitation technique of the wound-field motor utilizing space harmonic is roughly divided into two types, the former being a three-phase distributed winding stator composed of winding pitches that intentionally generate second order space harmonic [28]. The latter is a three-phase concentrated winding stator type in which a second order space harmonic is inevitably generated due to the stator structure. On the other hand, according to the Ref. [29] complied by the Ministry of Economy, Trade and Industry of Japan, IM for industrial applications has a large loss ratio of armature copper loss about 40%, it can be expected that the effect

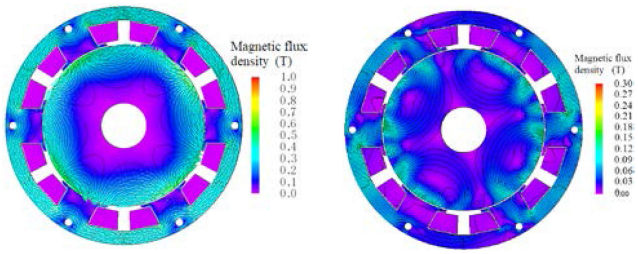

(a) 2nd order space harmonic. (b) 5th order space harmonic.

Fig. 2. Space harmonic distribution.

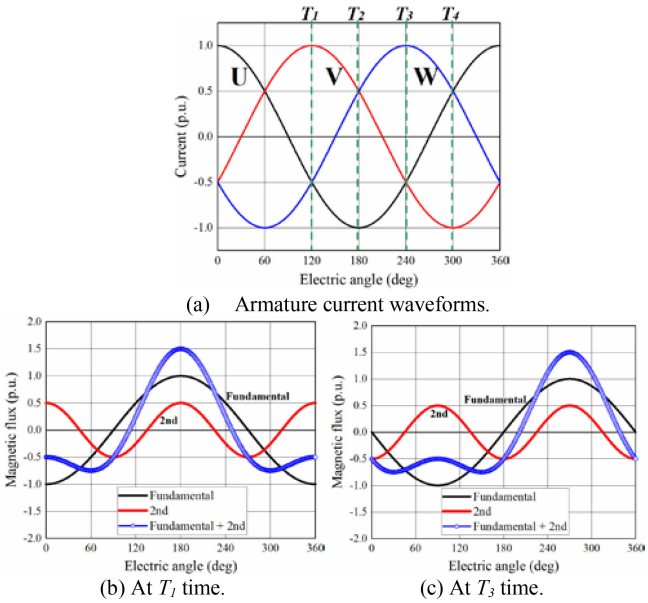

(a) Armature current waveforms.

(b) At T_1 time. (c) At T_3 time.

Fig. 3. Armature current waveforms and special magnetic force waveforms.

of improving the efficiency by reducing the armature copper loss by adopting the concentrated winding stator. Therefore, a magnetic circuit is designed based on the latter self-excitation technique using the three-phase concentrated winding stator.

Fig. 2(a) shows a magnetic flux density distribution of a second order space harmonic when a three-phase sinusoidal wave current is excited in the case where an iron solid rotor is combined in a concentrated winding stator. Fig. 3(b) shows spatial magnetomotive force waveform of the three-phase armature current at times T_1 and T_2 shown in Fig. 3(a). And, the waveforms obtained by separating the waveform into a fundamental wave and a second order harmonic. From both figures, the second order space harmonic is inevitably generated by the armature winding structure even when the sinusoidal wave is excited, and the harmonic is rotating magnetic field that moves in the opposite direction to the fundamental wave. In order to obtain a strong field flux during synchronous driving, an auxiliary pole is provided between salient poles to reduce the magnetic resistance against the second order space harmonic in Fig. 2(a).

Next, a secondary conductor bar is embedded in the rotor to obtain torque from the slip frequency during asynchronous drive. On the other hand, as described above, during synchronous

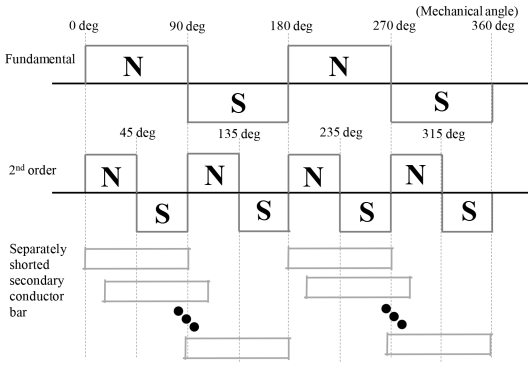

Fig. 4. Separately shorted secondary conductor bar with pole-pitch.

driving, the second order space harmonic is used as an energy source for non-contact power supply to the rotor windings. Therefore, when the slip $s = 0$, the magnetic coupling between the secondary conductor bar and the second order space harmonic should be set to zero. From above reason, if the secondary conductor bar connection pitch is set to pole pitch, the secondary current does not flow at $s = 0$. However, in the case of a structure in which the secondary conductor bar is entirely short-circuited by an end ring used in a general squirrel-cage type, a secondary current is generated due to magnetic coupling with the second order space harmonic during synchronous driving. Therefore, as shown in Fig. 4, the two conductor bar pairs are short-circuited at the pitch of the fundamental wave, and the two conductor pairs are electrically independent of the other pairs. The reason why the number of the secondary conductor bars is set to 40 in this prototype is determined so that the magnetic resistance is increased with respect to the fifth space harmonic shown in Fig. 2(b). Not only the second order space harmonic but also the fifth space harmonic are unavoidably generated by the stator structure, but this order causes iron loss and an increase in torque ripple. Furthermore, since it is not used for self-excitation, it must be reduced. In this prototype, the cross-sectional shape and embedding position of the secondary conductor bar are not magnetically optimized because of the principle verification stage and are determined from the assemblability of the prototype described later. In the future, there is a possibility that the optimization of motor parameters will be sufficiently studied. In particular, since the cross-sectional area of the secondary conductor bar is related to the resistance of the secondary conductor, it has a great influence on the slip which is the maximum torque point in the slip-torque characteristics.

Next, the respective connection methods of the rotor winding and the armature winding will be described. Since this motor is a line-start type self-excited wound-field motor, as described above, after self-starting by obtaining a starting torque from the slip frequency, it is necessary to form a field pole utilizing space harmonic and drive synchronously. Therefore, it is necessary to form a field pole immediately after accelerating to the synchronous speed. When it takes time to form the field pole, pulsation of the field flux occurs, and torque ripple increases. Further, if the pulsation of the field current occurs even after the formation of the field poles, the pulsation of the field flux leads

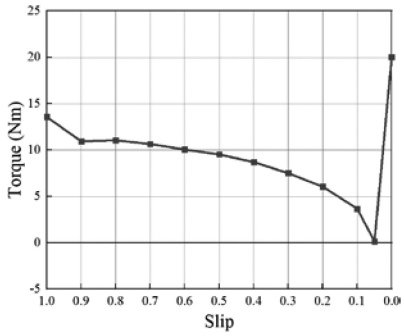

Fig. 5. Slip-*vs.*-torque characteristics under 100 $V_{\rm rms}$. (FE-analysis results).

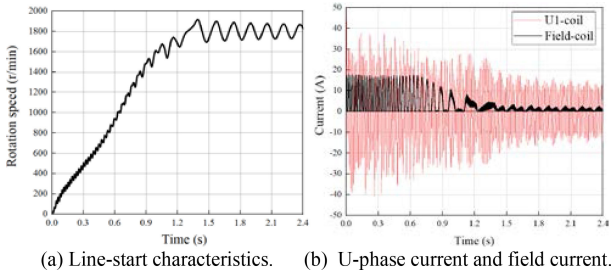

(a) Line-start characteristics. (b) U-phase current and field current.

Fig. 6. U-phase and field current at applied voltage 70.7 $V_{\rm rms}$ under no-load line start. (FE-analysis results).

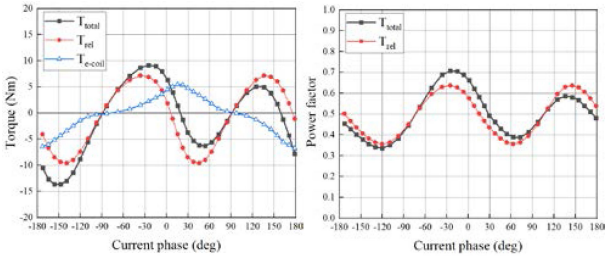

(a) Current phase-*vs.*-torque characteristics. (b) Current phase-*vs.*-power factor Characteristics.

Fig. 7. Synchronous drive characteristics with respect to current phase at applied voltage 70.7 $V_{\rm rms}$. (FE-analysis results).

to an increase in the torque ripple. An increase in the torque ripple leads to an increase in the speed ripple, and as a result, an increase in the transient time until the synchronous rotation speed is settled or a failure the synchronous pull-in occurs. On the other hand, since this motor based on self-excitation technique, the time for forming a certain field pole after reaching the synchronous speed is determined by the time constant τ_r of (1) consisting of the rotor winding inductance L_r and the rotor winding resistance R_r.

$$\tau_r = \frac{L_r}{R_r} \tag{1}$$

Further, considering the mutual inductance, the armature winding inductance is also an important design parameter. Therefore, it is desirable that this motor has a low inductance design. Based on the above, the armature windings are connected in full parallel (two parallels), the rotor windings are connected to one rotor rectifier circuit in pole pairs, and two common cathode type diodes are provided on the rotor. The two diodes are mounted at the positions 180 degrees opposites each other to improve dynamic balance.

C. Asynchronous / Synchronous -vs.- Torque Characteristics by FE-Analysis

In this section, the torque characteristics of the proposed motor when it is asynchronous and when it is synchronous are clarified by electromagnetic field analysis. At first, in order to analyze how the torque characteristics with respect to slip change, the slip-*vs.*-torque characteristics of the proposed motor were obtained by electromagnetic field analysis (Used JMAG-Designer *ver.* 17, by JSOL Corp.). Fig. 5 shows the results calculated by FE-analysis. The simulation is a two-dimensional model, which is the result when 100 $V_{\rm rms}$ is applied with a 60 Hz three-phase sinusoidal current source. The torque at each slip is determined by setting the rotor rotation speed to a constant speed at each speed. From this figure, it can be confirmed that the torque has dropped significantly immediately before synchronization. Fig. 6 shows the simulation results of the rotation speed characteristics, U-phase current, and field current waveforms when line-start with no-load at the applied voltage of 70.7 $V_{\rm rms}$. Here, U1-coil means the current flowing through one U-phase coil of the armature windings connected in parallel. In this figure, the synchronous speed is reached from about 1.3 s. At this time, the AC component is generated in the field current even during the asynchronization, and a single-phase alternating magnetic field is generated due to the rotor winding circuit configuration. In the future, it is necessary to perform a more detailed analysis of the effect of this AC component on the torque characteristics when not synchronized. Specifically, in the future, it will be necessary to measure the slip-*vs.*-torque characteristics with an actual machine and to measure and analyze the field current through a slip ring. In addition, considering the proportional shifting characteristics, it is expected that the torque characteristics immediately before synchronization will be improved by adjusting the value of the secondary conductor resistance in the specifications of this prototype to be a little smaller. This is a subject for consideration in the future works.

Next, Fig. 7(a) shows the synchronous drive characteristics when the applied voltage phase is changed by the three-phase sinusoidal wave voltage source at applied voltage 70.7 $V_{\rm rms}$. The current phase in this figure is obtained from the result of the voltage source analysis, and the current phase reference (0 deg) is the $+q$-axis in the dq-axis coordinates. The rotation speed of the rotor is constant at a synchronous speed (1800 r/min). In this figure, T_{rel} is the reluctance torque of the proposed motor, $T_{e\text{-}coil}$ is the self-excited electromagnet torque, T_{total} is the synchronous torque, and $T_{total} = T_{rel} + T_{e\text{-}coil}$, respectively. More accurately, it is conceivable that an induction torque, which is a braking torque, is generated by the odd-numbered space harmonics interlinking with the secondary conductor bar during synchronization. However, it is ignored because it is difficult to separate the its torque. T_{rel} is the simulation result with the rotor winding open, and $T_{e\text{-}coil}$ was calculated approximately

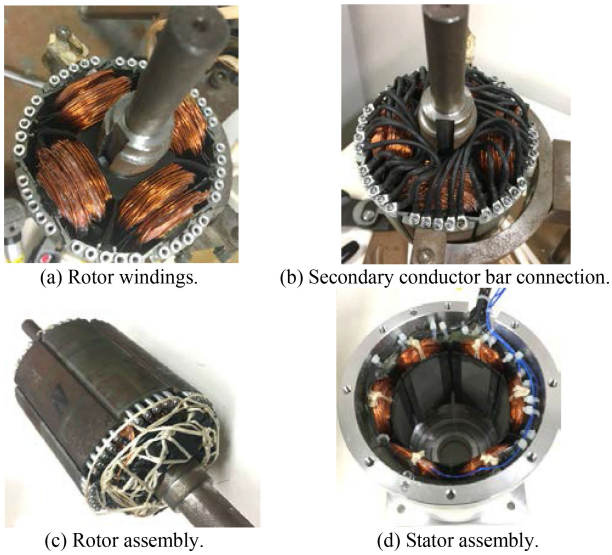

(a) Rotor windings. (b) Secondary conductor bar connection.

(c) Rotor assembly. (d) Stator assembly.

Fig. 8. Actual prototype machine.

by subtracting T_{rel} from T_{total}. As can be seen from Figs. 1(a) and (b), since the proposed motor is a forward salient pole type, the reluctance torque becomes positive in the flux intensifying region. The self-excited electromagnet torque is maximum at about 15 deg in the flux weakening region, not at 0 deg on the $+q$-axis. This is because the interlinkage amount of the second-order space harmonic to the I-coil changes depending on the armature current phase [26]. Next, Fig. 7(b) shows the power factor characteristics. It can be seen that the power factor is improved by forming a field flux in the rotor by self-excitation. These results show that the proposed motor can utilize reluctance torque and electromagnet torque during synchronization, and has the potential to improve the allowable load torque over IM and LS-PMSM. In the future, it will be necessary to measure these characteristics using a load motor in an actual machine and evaluate them experimentally.

D. Prototype

Fig. 8 shows a prototype. With the auxiliary pole removed, an AIW conductor with a wire diameter of ϕ0.8 was wound around the salient pole as I-coil and F-coil, and then the auxiliary pole was attached and assembled as shown in Fig. 8(a). From the viewpoint of assemblability, the rotor core and the auxiliary pole are made of an electromagnetic steel sheet laminated by bonding. The insulation between the rotor windings and the iron core is secured by a 0.5 mm thick cover made with a CFRP 3-D printer. The space factor of the rotor winding is 21.5% for I-coil and 45.7% for F-coil due to the limitation of the coil-end length and the trial production by hand winding. Next, the secondary conductor bar is connected as shown in Fig. 1 (c). Here, the secondary conductor bar is cut into a cylindrical shape of ϕ3.1 and taps for attaching M2-size screws in JIS standard are provide at both ends. After embedding the secondary conductor bar in the hole of iron core, using an AIW round wire with a wire diameter of ϕ1.1, both ends of the secondary conductor were short-circuited with round terminals and M2-size screws as shown in Fig. 8(b). Next, using a TO-247 standard common cathode SiC diode on the rotor, one pole pair is connected by the rectifier circuit shown in Fig. 1(d), and the rotor is prototyped as shown in Fig. 8(c). The rotor windings and the circuits on the rotor windings were fixed using resin to prevent centrifugal force, improve mechanical strength against electromagnetic force, and strengthen insulation between the windings and the ion core. The inertia of the rotor was $J = 0.013198$ kgm^2 as a result of actual measurement by the two-point suspension method.

The stator was a split core with the aim of improving the ease of trial production and improving the space factor, and an AIW round wire with a wire diameter of ϕ0.8 was manually wound via a 0.9 mm insulating bobbin. The space factor is 41.5%. After being bolted to the stator housing as shown in Fig. 8(d), it was secured with resin in the same manner as the rotor to ensure mechanical strength and insulation between the winding and the core.

III. Experimental Test

In this section, in order to clarify the operation principle of the proposed LS-SEWFM, load tests are performed with a fan or with an eddy current brake as loads. In the case of the former, the load is low inertia and a very light, but the load increases with the cube of the rotation speed. In the latter case, the load is larger than in the former, and the load increases with the square of the rotation speed. Further, according to the eddy current brake principle, the larger the acceleration, the larger the load. Therefore, it is possible to verify the self-start characteristics due to the difference in the load characteristic.

A. Fan Loads

As shown in Fig. 9(a), two types of fans, a propeller type and an impeller type, were prototyped with a CFRP 3-D printer. Since the application of this research is intended for driving a fan and pump, the above two types of fans are used. Fig. 9(b) shows the actual setup. The prototype is driven by a commercial AC power supply while varying the voltage with a transformer via an electromagnetic breaker. The line voltage V and phase current I are measured using a differential probe (Yokogawa 700925) and current probe (RIGOL RP1001C). The torque and rotation speed are measured using a torque meter (UNIPULSE UTM-II 20 Nm). Fig. 10 shows the measurement results of the rotation speed and torque with two fan types when the line start was performed under each applied voltage. Here, "Fan-1" is a propeller type and "Fan-2" is an impeller type. At the rotation speed shown in this figure, the sensor dead zone is less than 150 r/min, and therefore, it cannot be measured from immediately after the start until reaching 150 r/min. The sampling frequency of torque and rotation speed is 300 Hz depending on the device specifications.

As can be seen from this figure, if the self-starting is performed in the state where the applied voltage V is low, the synchronization cannot be pulled in, the motor is driven by IM, and the motor rotates at asynchronous rotation speed. In this figure (b) and (c), it can be confirmed that, when the proposed motor is started with an enough applied voltage, it can rotate synchronously at

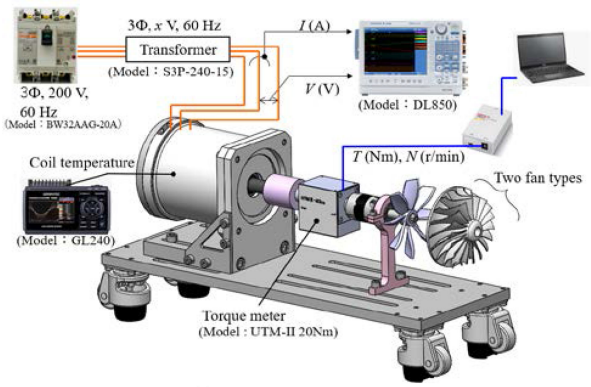

(a) Measurement setup.

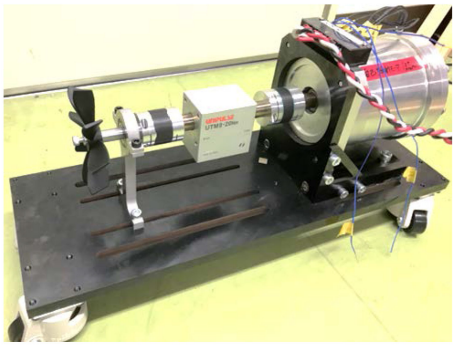

(b) Actual setup with propeller type fan.

Fig. 9. Experimental setup.

1800 r/min, which is the synchronous speed of 4-pole machine at a commercial frequency of 60 Hz. In case of impeller fan, as in the case of the propeller type, the synchronization can be pulled in from an applied voltage of about 110 V_{rms}. On the other hand, the torque ripple is larger in the case of the impeller type. This is because the impeller type has a larger windage loss and large thrust force is generated.

Fig. 11 shows the results obtained by organizing the losses excluding the mechanical loss with respect to applied voltage. In this figure, copper loss means Joule loss in a stator winding, and iron loss is a value obtained by subtracting copper loss from total loss. That is, the iron loss includes a secondary copper loss in the rotor windings, a loss in the secondary conductor bar, a conduction loss of the diode, which are difficult to separate by actual measurement. The mechanical loss was measured by the coasting method and is as shown in Fig. 12. It can be seen from Fig. 8 that the loss increases at a voltage slightly lower than the applied voltage that can be synchronized. Specifically, it is about 90 V_{rms} with the slip $s = 0.11$ just before the synchronization. From the Fig. 5, the torque has decreased significantly at the rotation speed immediately before the synchronization, especially around the slip $s = 0.05$. From this result, it is considered that the increase of the loss at $s = 0.11$ in the experimental result of Fig. 11 is due to the increase of the armature current to compensate for the decreasing torque. This can also be said from the experimental results shown in Fig. 10(b) and (c), where the torque value immediately before synchronization is greatly reduced.

B. Eddy Current Brake Loads

The load was changed to the eddy current brake in the same experimental environment in the case of fan loads. As shown in Fig. 13, the eddy current brake uses an 8-pole type for a light load and a 14-pole type having a larger load. As shown in Fig. 13(a), the rotor consists of a magnet (residual magnetic flux density $B_r = 60$ mT for 8 pole), carbon steel (S45C), for the rotor yoke, and a housing prototyped with a CFRP 3-D printer. The 8-pole rotor has a mass of 460 g. The gap between the rotor and the stator is 1.5 mm. The stator was made of three different materials: rolled steel (SPCC), carbon steel (S45C), and aluminum plate (A2017) in Japanese Industrial Standards, respectively to verify performance due to differences in load characteristics. In other words, in the case of A2017 material, it acts as a load that suppresses torque ripple due to the action of attenuating magnetic flux fluctuations. On the other hand, in the case of SPCC and S45C, the magnetic attraction between the magnet and the iron core causes a large torque fluctuation load, and the load characteristics against slip differ depending on the electrical resistivity of the two materials. The eddy current brakes are mainly for a load experiment that simulates a fluid element of the pump load.

Fig. 14 shows the line start characteristics of the rotation speed and the torque at each applied voltage when an 8-pole eddy current brake is used as a load. In this figure, the applied voltage is the average value when three loads were tested. Here, the reason why the applied voltage is slightly different is that the dial of the transformer cannot be reproduced every time because the dial is manually set. In this figure, as in the case of the fan load, the torque ripple and the rotation speed ripple also tend to increase near the synchronous speed. Further, by carefully checking the change in speed with time, it is confirmed that the acceleration increases from the middle area between zero and synchronous speed. At this time, the load torque dropped from about 0.3 Nm to 0.4 Nm. In other words, from slip-*vs*.-torque characteristic of the eddy current brake, the load torque increases as the time change of the magnetic flux increases. Therefore, the load torque is large at the line start. In addition, at the synchronous speed, the speed difference between the stator and the rotor of the eddy current brake becomes the largest, so that the load torque becomes large. From this, the load torque fluctuation due to the flow rate fluctuation of the pump application can be approximately simulated by using the eddy current brake of magnet excitation as the load. Fig. 15 shows the results of the loss measurement in the same manner as the fan load. As with the fan load, when the applied voltage immediately before synchronization, the armature current increases due to an increase in torque ripple and a decrease in torque. Further, since the field current ripple is considered to increase, the loss increases. At a synchronous speed of about 130 V_{rms}, the armature current increases due to the increase in the applied voltage, and the copper loss increases.

Next, the results of the 14-pole model with the eddy current brake will be described. The brake magnet has a residual magnetic flux density of 180 mT, and the rotor has a mass of 418 g. From the results of the 8-pole model, it was confirmed that the synchronous pull-in can be performed even if the load

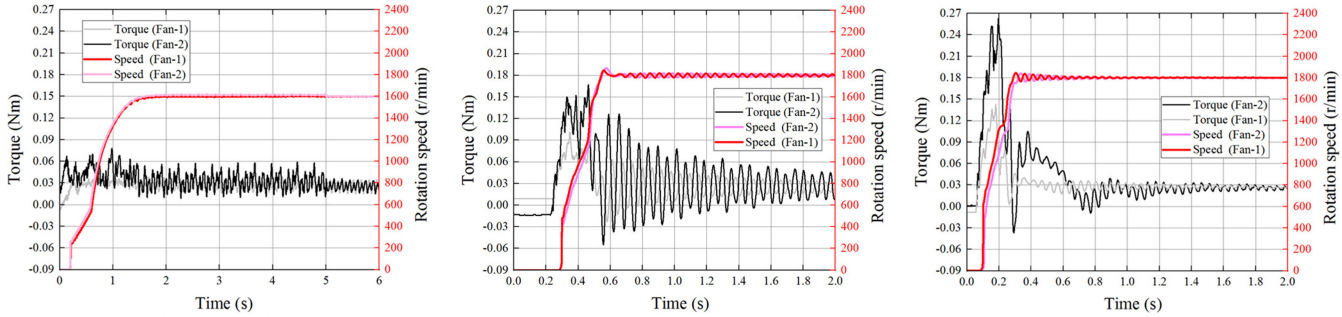

(a) Applied voltage at 58.2 V_{rms}. (b) Applied voltage at 110.3 V_{rms}. (c) Applied voltage at 129.9 V_{rms}.

Fig. 10. Line start characteristics with respect to applied voltage under fan loads.

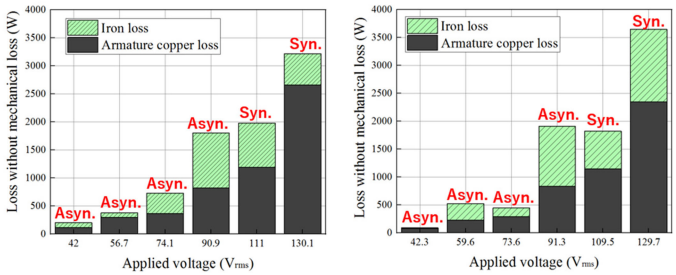

(a) Fan-1. (b) Fan-2.

Fig. 11. Measured loss with respect to applied voltage under fan loads.

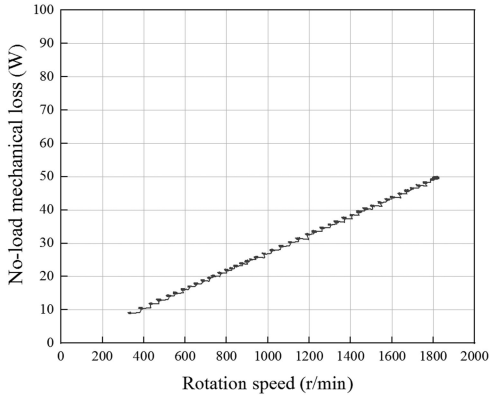

Fig. 12. Mechanical loss at no-load.

characteristics of the eddy current brake are different, so this time, A2017 material, which has the largest load, is used as the stator.

Fig. 16 shows load characteristics of the torque and rotation speed at each applied voltage. In the case of 8-pole model, the load under synchronous speed was a maximum of about 0.25 Nm in steady state. However, by increasing the number of poles to 14 poles, this experiment can be performed with a load of a maximum of about 0.5 Nm in steady state. When the load increases, the voltage that can be synchronized increases. With the 8-pole model, the applied voltage could be synchronized was about 110 V_{rms}, but with the 14-pole mode, it was synchronized from about 120 V_{rms}. Despite that the load slightly increased from 0.25 Nm to 0.5 Nm, the applied voltage that can be synchronized increased by about 10 V_{rms}. From this, it can be inferred that the torque is greatly reduced immediately before the synchronization speed. Also, in the time change of the rotation speed, the acceleration increases at a certain speed as in the case of another load. Further, as the applied voltage increases, the speed ripple is almost eliminated within the band of the sampling frequency 300 Hz. Nevertheless, it can be confirmed that the torque ripple is larger at the applied voltage immediately before the synchronization. The torque ripple or speed ripple is probably predicted to be inherent in the motor design due to rotor field current ripple. For further analysis, it is necessary to measure the rotor current in the future for further analysis. Fig. 17 shows the result of measured losses. The calculation method is the same as that for the fan load and the 8-pole model. From this figure, the loss tends to increase just before synchronization as with previous load results. Since the armature copper loss has increased, it can be said that an excessive armature current is flowing to compensate for the decrease in torque. In addition, it is necessary to analyze in detail the influence of the field current ripple on the loss. In the future, the protype will be modified so that the field current can be measured via the slip ring. Further loss separation will be performed by measuring the field current. As described previous section, the motor parameters have not been optimized in this stage for principle verification machine. Therefore, in this result, the effect of reducing the copper loss by the concentrated winding stator structure could not be confirmed so much, and the armature copper loss accounted for a large proportion of the loss. In designing motor that satisfies the required specifications in the next stage, it is important to strictly study the optimization of the balance of the field magnetomotive force and the armature magnetomotive force in order to improve efficiency.

C. *Effect of AC Component of Field Current on Starting Characteristics*

It has already been shown in Fig. 6 that the large AC component of the field current is generated during the non-synchronization. Experimentally verify how the AC component of the field current affects the starting characteristics. As a verification method, the connection of the secondary conductor bar is opened as shown in Fig. 18(a) and (b), and self-starting is performed in a state where no induced current flows in the

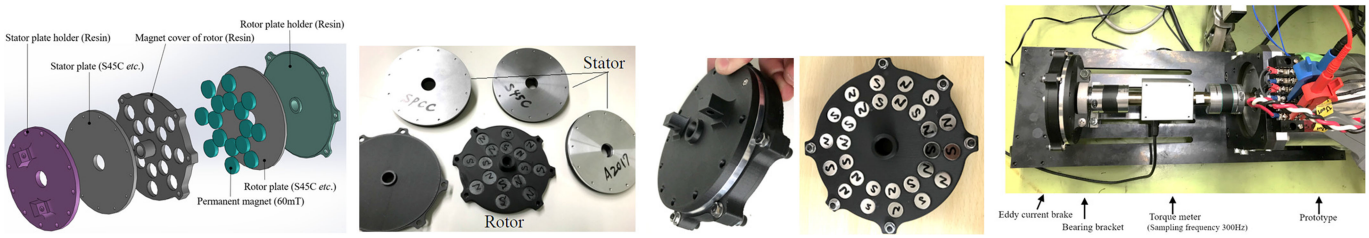

(a) Structural design of eddy current brake. (b) 8-pole rotor and stator of eddy current brake. (c) Eddy current brake Assembly. (d) Rotor of 14-pole Model. (e) Experimental setup with eddy current brake.

Fig. 13. Eddy current brake.

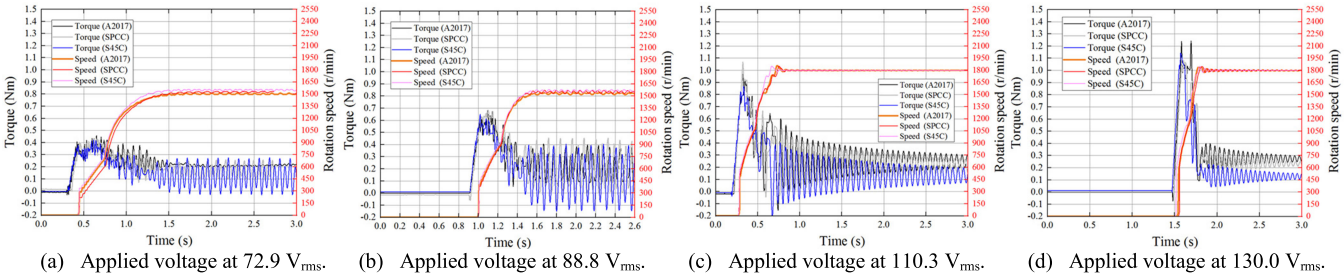

(a) Applied voltage at 72.9 V_{rms}. (b) Applied voltage at 88.8 V_{rms}. (c) Applied voltage at 110.3 V_{rms}. (d) Applied voltage at 130.0 V_{rms}.

Fig. 14. Line start characteristics with respect to applied voltage under 8-pole type eddy current brake loads.

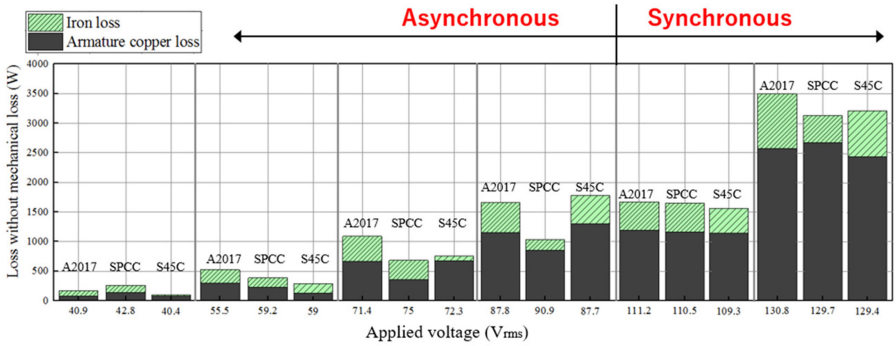

Fig. 15. Measured loss with respect to applied voltage under 8-pole eddy current brake loads.

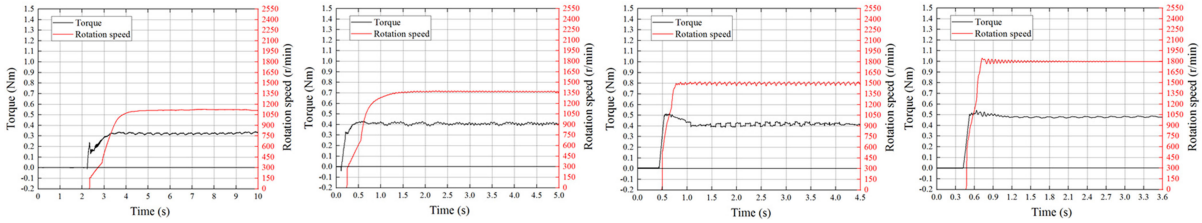

(a) Applied voltage at 57.1 V_{rms}. (b) Applied voltage at 72.4 V_{rms}. (c) Applied voltage at 103.8 V_{rms}. (d) Applied voltage at 118.9 V_{rms}.

Fig. 16. Line start characteristics with respect to applied voltage under 14-pole eddy current brake load.

secondary conductor bar. Then check if it can be rotated and synchronized. Fig. 18(c) and (d) show the results of experiments with a 14-pole eddy current brake load combined with a fan load and an A2017 stator. From these results, it can be confirmed that the induction torque is generated by the AC component of the field current even without the secondary conductor bar, and self-starting and synchronization can be performed. The rectifier circuit of the rotor winding has a single-phase alternating magnetic field. Here, from the theory of the two-rotating magnetic field, considering two rotating magnetomotive forces

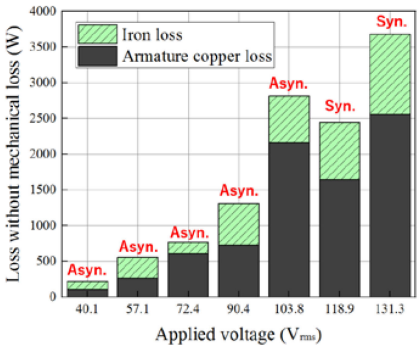

Fig. 17. Measured loss with respect to applied voltage under 14-pole eddy current brake load.

(a) Fastening bolt for secondary Conductor bar.

(b) Opened secondary conductor bar.

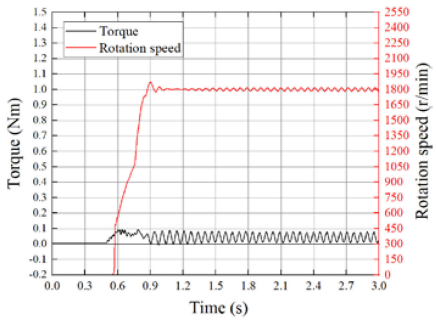

(c) Line-start characteristics with propeller type fan load at applied voltage 109 V_{rms}.

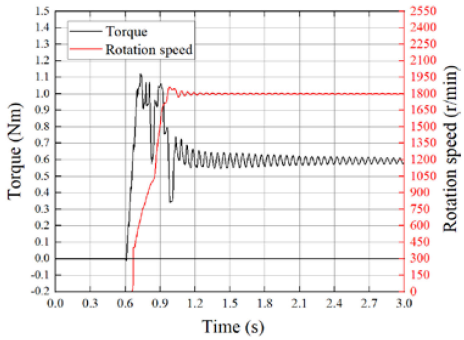

(d) Line-start characteristics with 14-pole eddy current brake load combined with A2017 stator at applied voltage 130 V_{rms}.

Fig. 18. Rotor with secondary conductor bar open and measured Line-start characteristics with its rotor.

that rotate in positive and negative phases, it is considered that the induction torque is generated in the positive phase component. Like the LS-PMSM, the DC-component of the field current and the negative phase component of the AC component produces braking torque when it is not in sync, but the proposed motor can utilize the positive phase component of the AC component as torque. The results show the potential for improved starting characteristics over IMs. On the other hand, from this result, the following can be considered about the drop of the torque just before the synchronous speed described in Section II-C in Fig. 5. The torque drops due to the generation of the braking torque by the DC-component of the field current and the negative phase component of the AC component. As future work, it is necessary to experimentally analyze the factors by comparing the harmonic analysis results of the speed ripple and torque ripple with the field current harmonic analysis results by directly measuring the field current via a slip ring.

IV. Conclusion

In this paper, for a general-purpose industrial motor that starts directly, the motor is accelerated by obtaining the starting torque from the slip frequency immediately after the line start, and is brushless to the rotor winding utilizing the second order space harmonic as the field energy source during synchronization. A new LS-SEWFSM was proposed and the downsized prototype was setup, and the load test was demonstrated to measure the rotation speed and torque characteristics and evaluate the loss. Through these results, the verification of the operation principle of the proposed LS-SEWFM and line-start characteristics were clarified. From the above, the following findings were obtained:

1) Based on the principle of the proposed motor, it obtains a starting torque from the slip frequency and accelerates, and at the time of synchronization, it can be driven as a wound-field type synchronous motor by organizing the field pole with second order space harmonic and rotor rectifier circuit.
2) At the synchronous speed, the allowable load torque may be improved by the two torques of reluctance torque and self-excited electromagnet torque.
3) Forming field poles in the rotor by self-excitation during synchronization may improve the power factor compared to IM.
4) In the non-synchronized state, the induction torque can be generated by the positive phase component of the AC component of the field current, and there is a possibility that the starting characteristics can be improved as compared with other line-start type motors.
5) At the rotation speed immediately before the synchronization speed, the torque greatly decreases, and the torque ripple also increases. Since the armature current increases in order to compensate of the decrease in torque, the armature copper loss increases.
6) The following can be said from the load test results using an eddy current brake that simulates the fluid elements of the pump and flow rate fluctuations. The proposed motor can synchronously pull in according to the principle even when the flow rate changes, or the load fluctuates.

This paper has verified that the LS-SEWFM self-starts according to the proposed principle with the actual machine. In the future, it is necessary to optimize the magnetic circuit and experimentally clarify the performance comparison with other

types of line-start motor such as a high-efficiency induction motor, a LS-SynRM, and LS-PMSM. In the next stage, based on the knowledge obtained in this research, we intend to develop a new motor that satisfies the IE4 efficiency standards of Japan for industrial general-purpose motors of several kW. In addition, as a future work, it is necessary to verify the FE-analysis results shown in Section II-C with actual equipment. Specifically, the prototype will be modified so that the rotor current can be measured via the slip ring. Then, the asynchronous torque characteristic and the synchronous torque characteristic are experimentally clarified by using the load motor.

REFERENCES

[1] C. M. Stephens, G. B. Kliman, and J. Boyd, "A line-start permanent magnet motor with gentle starting behavior," in *Proc. Conf. Record IEEE Ind. Appl. Conf. Thirty-Third IAS Annual Meet. (Cat. no. 98CH36242)*, St. Louis, MO, USA, 1998, vol. 1, pp. 371–379.

[2] Y. Bao, W. Mehmood, and X. Feng, "Super premium efficiency line start permanent magnet synchronous motor: Design, test and comparison," in *Proc. Petroleum Chem. Ind. Conf.*, Chicago, IL, 2012, pp. 1–7.

[3] R. T. Ugale and B. N. Chaudhari, "Rotor configurations for improved starting and synchronous performance of line start permanent-magnet synchronous motor," *IEEE Trans. Ind. Electron.*, vol. 64, no. 1, pp. 138–148, Jan. 2017.

[4] C. Debruyne *et al.*, "Evaluation of the efficiency of line-start permanent-magnet machines as a function of the operating temperature," *IEEE Trans. Ind. Electron.*, vol. 61, no. 8, pp. 4443–4454, Aug. 2014.

[5] S. Akita, T. Higuchi, Y. Yokoi, H. Saikusa, T. Abe, and S. Makino, "Experimental characteristics of a line-start permanent magnet motor," in *Proc. 19th Int. Conf. Elect. Mach. Syst.*, 2016, pp. 1–4.

[6] W. N. Fu and Y. Chen, "A post-assembly magnetization method for a line-start permanent-magnet motor," in *Proc. IEEE Trans. Appl. Supercond.*, Jun. 2016, vol. 26, no. 4, Art no. 0602604.

[7] J.-J. Lee, Y.-K. Kim, S.-H. Rhyu, and I.-S. Jung, "Magnet shape design of 3-phase line-start permanent magnet motor for high efficiency," in *Proc. Int. Conf. Elect. Mach. Syst.*, 2013, pp. 125–128.

[8] K. Tsuboi, T. Takegami, I. Hirotsuka, and M. Nakamura, "A general analytical method for a three-phase line-start permanent-magnet synchronous motor," *IEE J. Trans. IA.*, vol. 131, no. 5, pp. 692–699, May 2011.

[9] S. Kahourzade, A. Mahmoudi, R. Ravji, and W. L. Soong, "Line-start axial-flux PM motors: Introduction of a new machine topology," in *Proc. IEEE Energy Convers. Congr. Expo.*, Baltimore, MD, USA, 2019, pp. 7027–7034.

[10] A. Mahmoudi, S. Kahourzade, N. A. Rahim, W. P. Hew, and M. N. Uddin, "Design, analysis, and prototyping of a novel-structured solid-rotor-ringed line-start axial-flux permanent-magnet motor," *IEEE Trans. Ind. Electron.*, vol. 61, no. 4, pp. 1722–1734, Apr. 2014

[11] Y. Zhao, D. Li, M. Lin, and R. Qu, "A novel dual stator line-start permanent magnet synchronous machine," in *Proc. 2019 IEEE Int. Elect. Mach. Drives Conf.*, San Diego, CA, USA, 2019, pp. 1526–1531.

[12] J. Shen, P. Li, M. Jin, and G. Yang, "Investigation and countermeasures for demagnetization in line start permanent magnet synchronous motors," *IEEE Trans. Magn.*, vol. 49, no. 7, pp. 4068–4071, Jul. 2013.

[13] W. Lu, H. Zhao, and S. Liu, "Demagnetization conditions comparison for line-start permanent magnet synchronous motors," in *Proc. 17th Int. Conf. Elect. Mach. Syst.*, 2014, pp. 48–52.

[14] Y. Zhao, D. Li, T. Pei, and R. Qu, "Overview of the rectangular wire windings AC electrical machine," *CES Trans. Elect. Mach. Syst.*, vol. 3, no. 2, pp. 160–169, Jun. 2019.

[15] T. Fukami, R. Miyamoto, T. Miyamoto, and F. Shibata, "Self-starting, self-excited brushless three-phase synchronous motor," (in Japanese), *T. IEE Jpn.*, vol. 114, no. 4, pp. 470–471, 1994.

[16] Y. Hu, B. Chen, Y. Xiao, J. Shi, L. Li, and X. Li, "Rotor design and optimization of the three-phase line-start synchronous reluctance motor," in *Proc. 22nd Int. Conf. Elect. Mach. Syst.*, Harbin, China, 2019, pp. 1–6.

[17] B. Wymeerschl, F. De Belie, C. B. Rasmussen, and L. Vandevelde, "The effect of design considerations on the synchronization capability limits of line-start permanent-magnet synchronous motors," in *Proc. XIII Int. Conf. Elect. Mach.*, 2018, pp. 988–994.

[18] B. Poudel, E. Amiri, and P. Rastgoufard, "Design and analysis of line start synchronous reluctance motor with dual saliency," in *Proc. IEEE Transp. Electrific. Conf. Expo.*, Long Beach, CA, 2018, pp. 385–388.

[19] M. Villani, M. Santececca, and F. Parasiliti, "High-efficiency line-start synchronous reluctance motor for fan and pump applications," in *Proc. XIII Int. Conf. Elect. Mach.* , 2018, pp. 2178–2184.

[20] D. Mingardi and N. Bianchi, "Line-start PM-assisted synchronous motor design, optimization, and tests," *IEEE Trans. Ind. Electron.*, vol. 64, no. 12, pp. 9739–9747, Dec. 2017.

[21] T. Marčič, B. Štumberger, and G. Štumberger, "Differential-evolution-based parameter identification of a line-start IPM synchronous motor," *IEEE Trans. Ind. Electron.*, vol. 61, no. 11, pp. 5921–5929, Nov. 2014.

[22] H. Liu and J. Lee, "Optimum design of an IE4 line-start synchronous reluctance motor considering manufacturing process loss effect," *IEEE Trans. Ind. Electron.*, vol. 65, no. 4, pp. 3104–3114, Apr. 2018.

[23] L. N. Tutelea, T. Staudt, A. A. Popa, W. Hoffmann, and I. Boldea, "Line start 1 phase–source split phase capacitor cage–PM rotor–Relsyn motor: Modeling, performance, and optimal design with experiments," *IEEE Trans. Ind. Electron.*, vol. 65, no. 2, pp. 1772–1780, Feb. 2018.

[24] A. Castagnini, T. Känsäkangas, J. Kolehmainen, and P. S. Termini, "Analysis of the starting transient of a synchronous reluctance motor for direct-on-line applications," in *Proc. IEEE Int. Elect. Mach. Drives Conf.*, Coeur d'Alene, ID, 2015, pp. 121–126.

[25] E. G. Shehata, "Design tradeoffs between starting and steady state performances of line-started interior permanent magnet synchronous motor," in *Proc. 7th IET Int. Conf. Power Electron. Mach. Drives*, 2014, pp. 1–6.

[26] M. Aoyama and T. Noguchi, "Permanent-magnet-free-synchronous motor with self-excited wound-field technique utilizing space harmonics," in *Proc. IEEE Appl. Power Electron. Conf. Expo.*, Tampa, FL, 2017, pp. 3187–3194.

[27] K. Aiso and K. Akatsu, "Proposal and machine characteristics of a single-phase SRM driven by commercial AC power supply," *IEE J. Trans. IA.*, vol. 135, no. 11, pp. 1091–1099, 2015.

[28] F. Shibata and T. Fukami, "A brushless and exciterless polyphase synchronous motor," *IEEE Trans. Energy Conversion*, vol. EC-2, no. 3, pp. 480–488, Sep. 1987.

[29] Jun. 2014. [Online]. Available: https://www.meti.go.jp/committee/sougouenergy/shou_energy_kijun/sansou_yudou/report_01.html

Masahiro Aoyama (Member, IEEE) was born in Shizuoka, Japan, in 1984. He received the bachelor's degree in electric engineering from the Nagaoka University of Technology, Nagaoka, Japan, in 2006, the master's degree in advanced engineering course from Toyota Technical Institute, Nagoya, Japan, in 2008, and the D.Eng. degree in engineering from the Department of Environment and Energy System, Shizuoka University, Shizuoka, Japan, in 2015.

In 2008, he joined Suzuki Motor Corporation, Hamamatsu, Japan. After engaging in research on traction motors for electric vehicles, he retired in March 2018. Since April 2018, he has been an Assistant Professor with the Department of Electrical and Electronics Engineering, Shizuoka University, Hamamatsu, Japan. His research interests include electric machine design and its motor drives.

Dr. Aoyama is a member of the IEEE Power and Energy Society, Industry Applications Society and Industrial Electronics Society, and the Institute of Electrical Engineers of Japan.

Mitsuru Saito was born in Ibaraki, Japan, in 1997. He received the bachelor's degree in electrical and electronics engineering from Shizuoka University, Shizuoka, Japan, in 2020. Since April 2020, he has been studying in electrical and mechanical engineering program, Nagoya Institute of Technology, Nagoya, Japan. His research interests include electric machine design and its motor drives. He is a student member of the Institute of Electrical Engineers of Japan.

Takahiro Mizuta was born in 1988. He received the M.Eng. degree from the Department of Applied Physics, School of Engineering, University of Tokyo, Tokyo, Japan, in 2013. In 2013, he joined Advanced Technology R&D Center, Mitsubishi Electric Corporation, Hyogo, Japan, where he was involved in research and development of electric machines. He is a member of the Institute of Electrical Engineers of Japan.

Yoshihiro Miyama (Member, IEEE) was born in 1983. He received the M.Eng. degree from the Department of Science and Engineering, Ritsumeikan University, Shiga, Japan, in 2009, and the D.Eng. degree from Graduate School of Functional Control Systems, Shibaura Institute of Technology, Tokyo, Japan, in 2019. In 2009, he joined Advanced Technology R&D Center, Mitsubishi Electric Corporation, Hyougo, Japan, where he was involved in research and development of high-performance motor and its drive systems. Since 2020, he transferred to the Himeji Works, Mitsubishi Electric Corporation, Himeji, Japan, where he is developing traction motors for automotive applications. He is a member of the IEEE Industry Applications Society, and the IEE and SAE of Japan.

Kazumasa Ito was born in 1978. He received the master's degree in engineering from Nagoya University, Aichi, Japan, in 2002. In April 2002, he joined Advanced Technology R&D Center, Mitsubishi Electric Corporation, Hyogo, Japan, where he was involved in research and development of electric machines. In 2010, he transferred to Nagoya Works, Mitsubishi Electric Corporation, Aichi, Japan, where he developed the servo amplifier for factory automation. Since April 2013, he returned to Advanced Technology R&D Center. He was a corporate affiliate visiting fellow with the Walter H. Shorenstein Asia-Pacific Research Center (Shorenstein APARC), Stanford University, Stanford, USA, for academia year of 2017–2018. His research interests include high-performance electric motor and its drive systems. He is a member of the Institute of Electrical Engineers of Japan.